

G-equation modelling of thermoacoustic oscillations of partially premixed flames

Bernhard Semlitsch, Alessandro Orchini, Ann P Dowling and Matthew P Juniper

Abstract

Numerical simulations aid combustor design to avoid and reduce thermoacoustic oscillations. Non-linear heat release rate estimation and its modelling are essential for the prediction of saturation amplitudes of limit cycles. The heat release dynamics of flames can be approximated by a flame describing function. To calculate a flame describing function, a wide range of forcing amplitudes and frequencies needs to be considered. For this reason, we present a computationally inexpensive level-set approach, which accounts for equivalence ratio perturbations on flames with arbitrarily complex shapes. The influence of flame parameters and modelling approaches on flame describing functions and time delay coefficient distributions are discussed in detail. The numerically obtained flame describing functions are compared with experimental data and used in an acoustic network model for limit cycle prediction. A reasonable agreement of the heat release gain and limit cycle frequency is achieved even with a simplistic, analytical velocity fluctuation model. However, the phase decay is over-predicted. For sophisticated flame shapes, only the realistic modelling of large-scale flow structures allows the correct phase decay predictions of the heat release rate response.

Keywords

Thermoacoustic instability, non-linear combustion modelling, flame describing function, equivalence ratio perturbation

Date received: 26 September 2016; accepted: 2 May 2017

1. Introduction

A gas turbine combustor can behave as a self-sustained acoustic resonator.¹ Acoustic waves generated by unsteady combustion are reflected back towards their origin, causing unsteady heat release. If unsteady heat release occurs sufficiently in phase with pressure perturbations then periodic or quasi-periodic oscillations can be self-sustained. These oscillations can lead to undesirable consequences, such as flame blow off,² flashback,³ or even fatigue of the combustor. Lean-burn flames are particularly receptive to such thermoacoustic oscillations.⁴ Nevertheless, lean-burn flames are increasingly popular in combustion applications because they produce low NO_x emissions, which helps to comply with increasingly stringent legislation.

In gas turbines, thermoacoustic oscillations usually cannot be avoided for all operating conditions. However, safe operability can be assured as long as self-excited oscillations are restricted to tolerable amplitudes. These oscillation amplitudes are governed by the non-linear relation of driving and damping

processes. Ideally, potentially damaging thermoacoustic oscillations will be identified at an early stage in the design process. In order to be practical, this requires numerically efficient techniques (such as acoustic networks, see e.g. Stow and Dowling⁵) so that a wide range of designs can be screened. In such scenarios, flame describing functions (FDFs), $\mathcal{F}(F_A, f)$, being dependent on forcing amplitudes F_A and frequencies f , can be used to characterise the non-linear flame response (in terms of heat release rate \dot{q}) when forced with a harmonic perturbation

$$\frac{\dot{q}'}{\bar{q}} = \mathcal{F}(F_A, f) \frac{u'_B}{\bar{u}_B} = \mathcal{G} \cdot e^{i\varphi} \frac{u'_B}{\bar{u}_B} \quad (1)$$

Department of Engineering, University of Cambridge, Cambridge, UK

Corresponding author:

Bernhard Semlitsch, Department of Engineering, University of Cambridge, Trumpington Street, Cambridge CB2 1PZ, UK.
Email: bs564@cam.ac.uk



where \mathcal{G} is the gain, φ is the phase delay, and u'_B is the imposed velocity disturbance just upstream of the burner orifice. Overbars and primes denote mean averaged and Fourier transformed quantities, respectively. The FDF can be determined using experimental measurements or numerical simulations and expressed as the sum of time delays, $\Delta\tau$, with coefficients k_n

$$\mathcal{F}(F_A, f) = \frac{\dot{q}'/\bar{q}}{u'_B/\bar{u}_B} \approx \sum_{n=1}^N k_n(F_A) e^{-i2\pi f n \Delta\tau} \quad (2)$$

These parameters, k_n and $\Delta\tau$, relate the amplification of the heat release response to a disturbance generated by acoustic waves at the fuel injection location or flame base and being retarded by the disturbance convection time. The time delay constants can be found by $k_n(F_A) = g(n\Delta\tau, F_A)\Delta\tau$, where $g(t, F_A)$ is the impulse response of the flame, which is calculated by applying the one-sided inverse Fourier transform on the FDF. To reconstruct the FDF by the sum of time delays, the calculated time delay constants are substituted into equation (2)

$$\begin{aligned} \mathcal{F}(F_A, f) &= \int_0^{\infty} g(t, F_A) e^{-i\omega t} dt \\ &\approx \sum_{n=1}^N g(n\Delta\tau, F_A) e^{-i\omega n \Delta\tau} \Delta\tau \end{aligned} \quad (3)$$

The number of time delays, N , determines the resolution of the FDF over a given frequency range. Hence, the limit cycle amplitude can be predicted more accurately as N and the forcing amplitude discretisation increase. This is particularly evident for the complex flame shapes found in industrial applications (see e.g. Macquisten et al.⁶). Hence, highly resolved FDFs are desired to represent the non-linear flame dynamics.

Highly accurate but numerically expensive methods restrict the assessment to a few forcing amplitudes and frequencies, which might lead to an inappropriate overall description of the non-linear flame dynamics. Therefore, inexpensive numerical methods that can provide sufficiently accurate results to predict FDFs at many forcing amplitudes and frequencies are desired. Dowling⁷ demonstrated that FDFs obtained from a kinematic flame model can be used to predict thermoacoustic instabilities appropriately. Such kinematic flame models based on level-set methods are computationally inexpensive, because only essential features are incorporated. Methods presented by Graham and Dowling⁸ can be used even for relatively complex flame shapes but depend on severe assumptions to be computationally practical. The drawback of Graham

and Dowling's implementation, which was to track two flame surfaces in a Lagrangian sense, is the handling of flame-pinch events and the distinction of burned and unburned regions. Due to these shortcomings, the numerical effort becomes high for strongly wrinkled flames, which limits the investigation range.

The impulse response or sum of time delay coefficients, used in the numerical limit cycle predictions, reveals the timescales of the processes leading to a heat release rate modulation. Huber and Polifke,^{9,10} Komarek and Polifke,¹¹ Blumenthal et al.,¹² and Albayrak et al.¹³ were able to distinguish the contributions of different mechanisms influencing the heat release by analysing their contribution to the impulse response. It has been suggested by Huber and Polifke^{9,10} that gains larger than unity can only be achieved with a combination of positive and negative time delay coefficients. Blumenthal et al.¹² indicated that a negative contribution, corresponding to a phase shift, can be caused by restoration effects for premixed flames. Albayrak et al.¹³ extended this study by incorporating the effects of equivalence ratio perturbations. These findings highlight that physical insight can be gained by analysis of the time delay coefficients.

The main limitations of level-set methods modelling the non-linear heat release generated by flames have been the fragility to flame-pinch events, simplistic scenarios, and the lack of validation. In order to overcome these problems, we present a level-set method to estimate FDFs, which can robustly handle flame-pinch and sophisticated flames, such as an M-shaped flame. The computational efficiency of this approach allows evaluation of the flame response for numerous forcing amplitudes and frequencies. Therefore, the complexity of the heat release response can be integrated and analysed for many time delays and coefficients in acoustic network simulations. We describe the methodology to obtain the heat release rate from kinematic flame simulations in detail and emphasise the validation of the approach. The obtained results under different modelling assumptions are compared with available experimental data. Consequences of the modelling assumptions are pointed out and the results are examined critically.

2. Methodology – Flame front tracking

Assuming that chemical reactions between fuel and oxidiser occur instantaneously in a thin sheet, the flame front can be regarded as a discontinuity dividing reactants and products. The kinematics and surface alterations of the flame front determine its dynamic heat release response. The thin, flat flame burns normal to its front at the flame speed, which is determined by local chemical reaction rates.

A scalar G -field indicating the shortest distance to the flame front can be defined, where an arbitrary fixed value G_0 , e.g. zero, can be used to identify the flame front location. Values of G larger or smaller than G_0 represent the unburned mixture or products, respectively. By defining the scalar G -field to be smooth and continuous in the spatial domain, the normal \mathbf{n} pointing into the unburned mixture can be calculated by $-\nabla G/|\nabla G|$. Therefore, the convective motion of the flame front is dictated by the local flame speed s_L and the local flow velocity \mathbf{u} at which the reactants arrive. The material derivative of the level set describes the flame front movement by the so-called G -equation

$$\frac{DG}{Dt} = \frac{\partial G}{\partial t} + \left(\mathbf{u} - s_L \frac{\nabla G}{|\nabla G|} \right) \cdot \nabla G = 0 \quad (4)$$

With the integration of the implicit G -field, a fully non-linear description of the flame dynamics is obtained.

The flame speed s_L depends on the local equivalence ratio ϕ and curvature effects

$$s_L = c_0 s_L^0 (1 - \mathcal{L}\kappa) = c_0 c_1 \phi^{c_2} e^{c_3(\phi - c_4)^2} (1 - \mathcal{L}\kappa) \quad (5)$$

where s_L^0 is the burning speed of a flat flame, \mathcal{L} is the Markstein length, and $\kappa = \nabla \cdot \mathbf{n}$ is the local flame curvature. The fuel in the present investigation is ethylene and the flame speed, s_L^0 , as a function of the local equivalence ratio, ϕ , can be modelled by fitted factors c_i for the specific reactant media. The values for the coefficients are listed in Table 1. An additional constant c_0 is introduced (accordingly to the work by Graham and Dowling⁸) to alter the location of the numerically predicted flame front to that of the experimentally observed turbulent flame brush.

The unsteady heat release rate of an axisymmetric flame can be calculated by spatial integration along its front represented by the iso-surface $G=0$

$$\dot{q}(t) = 2\pi\rho c_0 s_L^0 \Delta h_R \iint (1 - \mathcal{L}\kappa) |\nabla G| \delta(G) r dr dz \quad (6)$$

The local enthalpy release $\Delta h_R(\phi)$ of the reaction per unit mass is defined as $\Delta h_R = 3.2 \cdot 10^6 (\min(1, \phi))/(1 + 0.067\phi) \text{ J kg}^{-1}$. A fast Fourier transform of the heat release rate fluctuations $\dot{q}(t) - \bar{q}$ is performed, in which the contribution at the fundamental forcing frequency is extracted to calculate the gain and phase decay as defined in equation (1).

2.1. Geometry and set-up

The geometry of the laboratory combustor illustrated in Figure 1 is selected for these simulations. It was

Table 1. Coefficients used for equation (5) to represent ethylene.

$c_0(-)$	$c_1(m/s)$	$c_2(-)$	$c_3(-)$	$c_4(-)$
1.51314	1.32176	3.11023	1.72307	0.36196

experimentally investigated by Balachandran.¹⁴ Therefore, comparison of the numerical results with experiments is permitted. The burner consists of a cylindrical pipe with varying cross-section and centred bluff body. At the combustion chamber exit, the flow discharges into quiescent ambient conditions. Self-excited thermoacoustic instabilities were not observed experimentally with a combustion chamber height of 80 mm. Therefore, it was extended to 350 mm to investigate limit cycles.

The fuel is injected through tiny holes around the circumference of the centre body, which are located 55 mm upstream of the burner orifice. The air is supplied far upstream, where the inlet pressure and temperature are assumed to be at ambient conditions in the simulations, i.e. 101,325 Pa and 299 K, respectively. The imposed inlet air mass flow rate ($\dot{m}_{air} = 0.005417 \text{ kg/s}$) is estimated such that a velocity of 10 m/s is reached at the burner orifice. The employed flame properties are chosen according to the fuel ethylene. The fuel mass flow rate is specified in terms of the equivalence ratio ϕ , which is a parameter in the simulations. The fuel is assumed to mix uniformly with the air at the injection location.

2.2. Flow field

Analytical flow and disturbance models meet the requirements for the present purpose and are computationally efficient. The axisymmetric potential flow model developed by Graham and Dowling⁸ is used, in which a spherical point source is placed 40 mm upstream of the burner orifice. This source location z_{sr} determines the directivity of the flow and spread angle of an annular jet exhausting the port. The distance to the spherical source can be expressed as $\xi = \sqrt{r^2 + (z - z_{sr})^2}$. The radial velocity component in the spherical coordinate system can be written in terms of the velocity potential P as $u_\xi = \partial P / \partial \xi$. In order to conserve continuity and to ensure irrotationality, the velocity potential needs to satisfy $\nabla^2 P = 0$. Solutions have the form $P = A_u \xi^n$, where particularly $n = -1$ satisfies these conditions. With $P = A_u / \sqrt{r^2 + (z - z_{sr})^2}$, the velocity components in the cylindrical coordinate system can be written as

$$u_r = \frac{-A_u r}{\sqrt{(r^2 + (z - z_{sr})^2)^3}} \quad (7)$$

and

$$u_z = \frac{-A_u(z - z_{sr})}{\sqrt{(r^2 + (z - z_{sr})^2)^3}} \quad (8)$$

The potential amplitude $\overline{A_u}$ can be determined such that a desired mean velocity $\overline{u_B}$ at the burner orifice is obtained

$$\overline{A_u} = -\overline{u_B} \left(\left(\frac{r_{B,out} + r_{B,in}}{2} \right)^2 + z_{sr}^2 \right) \quad (9)$$

where $r_{B,out}$ and $r_{B,in}$ are the outer and inner radii of the burner orifice, respectively. A velocity perturbation with sinusoidal form can be included into the velocity model by writing

$$A_u = \overline{A_u} \cdot (1 + F_A \sin(2\pi ft)) \quad (10)$$

where F_A is the forcing amplitude and f is the forcing frequency.

Secondly, we use the low-order model developed by Orchini and Juniper,¹⁵ a more realistic representation of the flow field and its perturbations. The time-averaged velocity distribution obtained by unsteady Reynolds averaged Navier–Stokes (uRANS) simulations (see Armitage et al.¹⁶) is employed as base flow, while two counterrotating vortical flow structures mimic the large-scale flow perturbations. The axial flow perturbations are convected from the burner mouth with the velocity at the mid-streamline, while the radial perturbations are determined by satisfying mass conservation.

2.2.1. Equivalence ratio perturbations. The fuel is injected at a location z_{inj} upstream of the burner orifice. Because the mixing process is not considered upstream of the flame, the reactant mixture distribution is passively convected by the mean flow from the injection to the reaction zone. The fuel mass flow rate is not significantly influenced by acoustic disturbances for still injectors¹⁷ and therefore equivalence ratio perturbations can be assumed to be inversely proportional to local air velocity fluctuations at the injector nozzle

$$\phi'_{inj} = \frac{\overline{u_{inj}} \bar{\phi}}{u'_{inj}} = \frac{\bar{\phi}}{(1 + F_A \sin(2\pi ft))} \quad (11)$$

The equivalence ratio oscillation ϕ'_B passing the burner orifice at time t can be expressed as $\phi'_B(r, z, t) = \phi'_{inj}(r, z, t - \tau)$, where τ represents the retarded time, which is required to convect the disturbance from the injection location to the burner orifice. From this point on, the convection of the equivalence ratio oscillation is simulated.

The mean retarded time can be calculated as $\bar{\tau} = \int_0^z \bar{u}^{-1} dz$, where \bar{u} is the mean velocity in the duct. Figure 1 illustrates the cross-sectional change of the duct due to the flame holder, which results in a flow acceleration. Therefore, the time delays are calculated for the straight annular duct and the section constricted by the bluff body separately. The convection distance past the flame holder is $|z_{fh}| = \left| \frac{r_{B,in} - r_{fh}}{\tan 45^\circ} \right|$, while the convection distance in the straight annular section is $|z_{an}| = |z_{inj} - z_{fh}|$ (r_{fh} is the inner radius of the annular duct). Since the flow can be assumed to be incompressible in the ducts, the flow velocities are proportional to cross-sectional variations

$$\overline{u_{an}} = \overline{u_B} \frac{(r_{B,out}^2 - r_{B,in}^2)}{(r_{B,out}^2 - r_{fh}^2)} \quad (12)$$

and

$$\overline{u_{fh}} = \overline{u_B} \frac{(r_{B,out}^2 - r_{B,in}^2)}{(r_{B,out}^2 - z^2 \tan^2(45^\circ))} \quad (13)$$

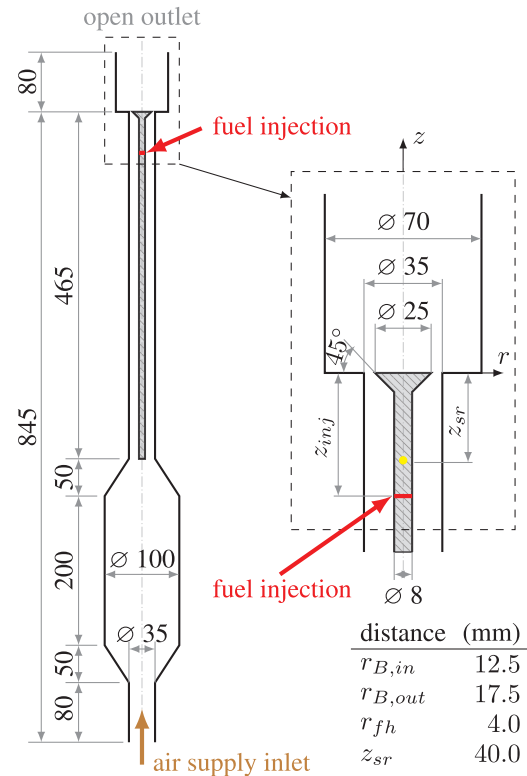


Figure 1. Sketch of the burner developed by Balachandran.¹⁴ All dimensions are in millimetres.

The retarded times for the two duct sections are

$$\overline{\tau}_{an} = \frac{r_{B,out}^2 - r_{fh}^2}{\overline{u}_B(r_{B,out}^2 - r_{B,in}^2)} \left(|z_{inj}| - \frac{(r_{B,in} - r_{fh})}{\tan 45^\circ} \right) \quad (14)$$

and

$$\overline{\tau}_{fh} = \frac{r_{B,in} - r_{fh}}{\overline{u}_B(r_{B,out}^2 - r_{B,in}^2) \tan(45^\circ)} \cdot \left(r_{B,out}^2 - \frac{(r_{B,in} - r_{fh})^2}{3} \right) \quad (15)$$

2.3. Implementation

The present implementation of the level-set solver originates from the work by Hemchandra¹⁸ and was developed further by numerous authors (see e.g. Kashinath et al.¹⁹ and Orchini and Juniper²⁰).

The extent of the computational domain is outlined in Figure 2. A regular two-dimensional grid of 441×441 nodes is employed for the numerical discretisation exploiting the axisymmetry of the M-shaped flame, where a grid sensitivity analysis was performed. The numerical mesh starts below the burner orifice in

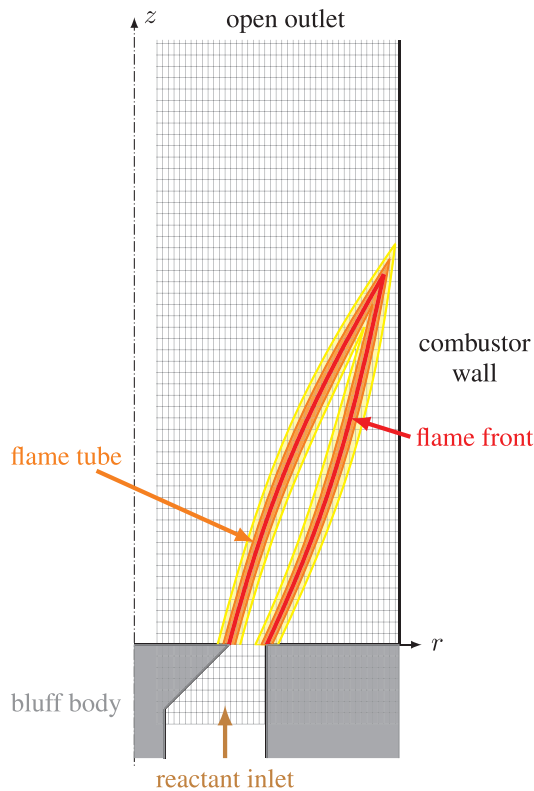


Figure 2. Sketch of the tubes surrounding the flame front, where the orange tube represents $|G| \leq \beta$ and the yellow tube $\beta < |G| \leq \gamma$. (The grid indicates the extent of the two-dimensional axisymmetric computational domain.)

order to facilitate the implementation of the flame boundary conditions at the lip. A strip at the centreline is excluded to reduce the computational effort.

The flow field can be calculated directly or is supplied (in case of the uRANS-based flow model) at initialisation. Further, a uniform equivalence ratio field (set to the mean equivalence ratio $\bar{\phi}$) and a smooth initial G -field satisfying the boundary conditions are provided. The steady-state flame evolving without perturbations is used as initial condition for every operating condition.

Executing an iteration, the flow field and velocity oscillations are calculated. The equivalence ratio fluctuations are convected throughout the domain, where a fifth order weighted essentially non-oscillatory WENO scheme is used for spatial discretisation and an implicit third-order Runge–Kutta total variation diminishing scheme is employed for time integration.

Equation (4) shows that the convection of the G -field is only dependent on the local flow velocity and flame speed. Therefore, only the near-field surrounding the flame front needs to be considered, which is illustrated in Figure 2 by an orange and a yellow region surrounding the red coloured flame. These represent the two concentric tubes around the zero level set with constant radii $0 < \beta < \gamma$ from the flame front, which are calculated initially and re-established after each iteration.^a The G -field is only convected in the interior of the narrower tube as a signed distance function, whereas constant extremal values are assigned beyond the outer tube. A smooth transition is computed in between the inner and outer tube. This can be expressed accordingly to Peng et al.²¹ as

$$\frac{\partial G}{\partial t} + c(G) \left(\mathbf{u} + \mathbf{s}_L \frac{\nabla G}{|\nabla G|} \right) \cdot \nabla G = 0 \quad (16)$$

where

$$c(G) = \begin{cases} 1 & \text{if } |G| \leq \beta \\ (|G| - \gamma)^2 \frac{(2|G| + \gamma - 3\beta)}{(\gamma - \beta)^3} & \text{if } \beta < |G| \leq \gamma \\ 0 & \text{if } |G| > \gamma \end{cases} \quad (17)$$

The spatial and time derivatives are computed with the same discretisation schemes as the equivalence ratio fluctuations, which were mentioned in the preceding paragraph. This so-called narrow band level-set method has been described in more detail by Peng et al.²¹ and Sethian.²²

Sharp gradients can evolve during the simulation advancement, as e.g. with pinching events. In order to keep the G -field smooth, re-initialisation steps are performed,²³ which consists essentially of solving the Eikonal equation $|\nabla G| = 1$. This procedure is

performed each time step before a gradient calculation of the updated G -field is required.

The computation of the heat release rate requires the integration at a level set $G=0$, where the numerical evaluation utilised the formulation by Smereka.²⁴ Since the flame tubes are used to track the flame front, the flame tubes are rebuilt with the updated information of the G -field after the core processes of the simulation have been performed. A high-order algorithm is used for integration of the flame surface, which is accomplished by using a one-step adaptive mesh refinement, subdividing each cell into five node points.

The unsteady heat release and flow velocity are the essential quantities to construct the FDF and are therefore saved every time step. The required statistical accuracy governs the simulation duration. Due to the modelling assumptions in the present simulations (absence of sources generating stochastic fluctuations), the heat release rate cycles evolve identically except for negligible errors caused by numerical uncertainty. Therefore, the computation duration can be restricted to the heat release response of the flame on one complete forcing cycle (after the transient). Nonetheless, repeatability has been ensured for the presented data by simulating at least eight full forcing cycles. Only data acquired after the initial transient are considered for the post-processing.

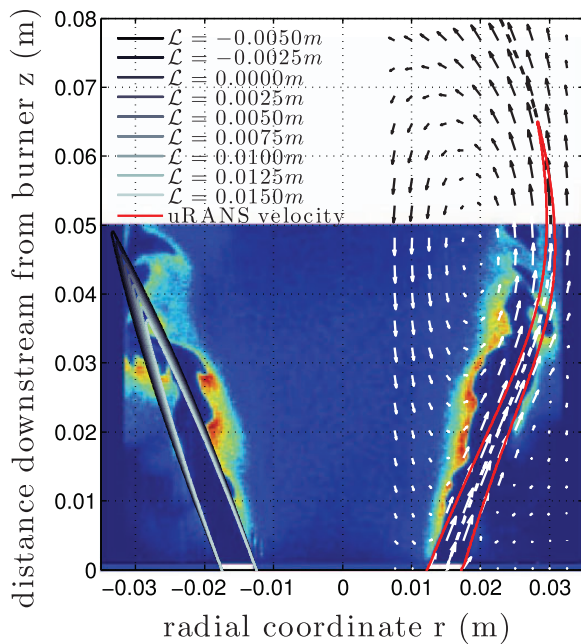


Figure 3. Unperturbed flame shape: the results with different flow field models (left: potential flow and right: uRANS time-averaged flow) at a mean equivalence ratio ϕ of 0.55 is compared with an instantaneous OH PLIF image (Balachandran,¹⁴ pp.72). uRANS: unsteady Reynolds averaged Navier–Stokes.

2.4. Validation, comparison to experimental data

The simulation results are compared to previously computed data by Graham and Dowling⁸ and experimental measurements obtained by Balachandran¹⁴ in order to investigate the validity and uncertainty of the approach.

First, the flame shape relies on many parameters, such as the velocity model, flame speed, and Markstein lengths and is compared to an experimental image of the flame in Figure 3. The inclination of the steady flame is estimated consistently. For the potential flow model, the best agreement in terms of flame length takes place when flame curvature effects are neglected. A perfect comparison, with overlapping curves, with respect to prior simulation data⁸ using an explicit G -equation modelling formulation was achieved. Using a uRANS mean flow field, the flame evolves narrower and more elongated. However, unsteady flow leads to a wrinkled flame shape even without forcing in the experimental set-up. These features are not represented

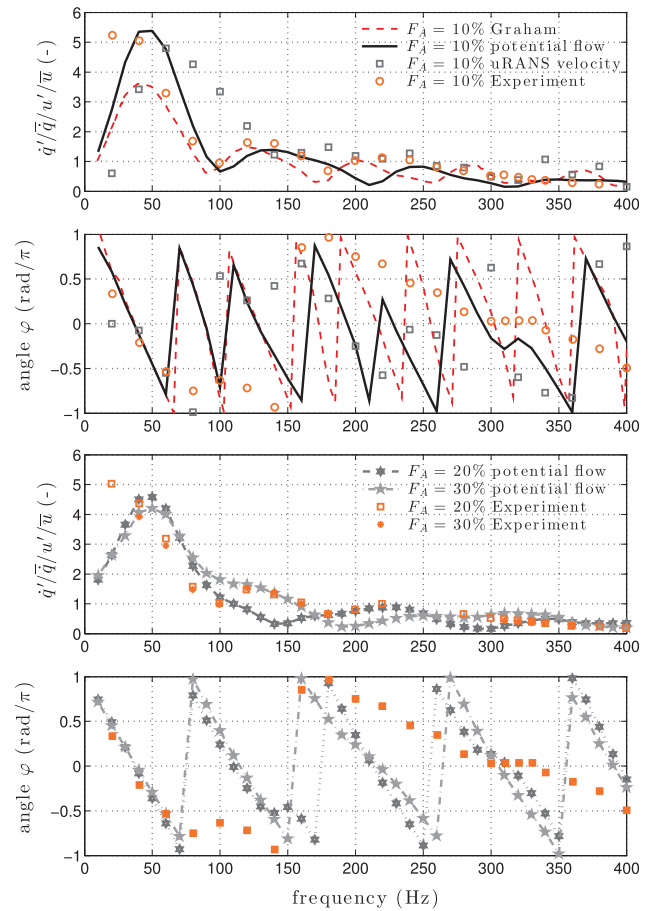


Figure 4. For different forcing amplitudes, F_A , the flame describing functions $\mathcal{F}(F_A, \omega)$ obtained with numerical and experimental methods are compared for a mean equivalence ratio ϕ of 0.55 without considering flame curvature effects.

in the flow models, which account only for forced flow disturbances.

FDFs have been measured experimentally in the range of 20–400 Hz and are compared to the present simulation results in Figure 4. Considering the simplicity of the potential velocity model, the prediction of the gain agrees reasonably with the measurements. Nevertheless, the phase decay is very rapid with the present approach at a forcing amplitude of 10% prior to flame pinching. For higher forcing amplitudes, the phase lag decays less steeply, but remains over-predicted compared with the experimentally evaluated behaviour. The highest gain shifted towards higher frequencies with the velocity model by Orchini and Juniper¹⁵ and incorporated equivalence ratio perturbations. Nonetheless, the phase decay is predicted similar as in the experimental data with the more realistic flow description.

Results by Graham and Dowling⁸ are highlighted in Figure 4 in order to illustrate the differences between Graham and Dowling's linearised G -equation model and the present approach with analytical flow model. In particular, the over-prediction of the phase lag is reduced at high frequencies (> 150 Hz), which can be attributed to the improved flame-pinching treatment with the implicit over the explicit G -field tracking approach.

The saturation behaviour as a function of the forcing amplitude has been measured for two forcing frequencies and is compared to the numerically predicted saturation amplitudes in Figure 5. For low forcing frequencies (< 100 Hz), good agreement is achieved at low forcing amplitudes. However, the heat release response is overestimated at high forcing amplitudes. An oscillatory behaviour of the heat release rate as a function of the forcing amplitude arises for higher forcing frequencies (> 100 Hz).

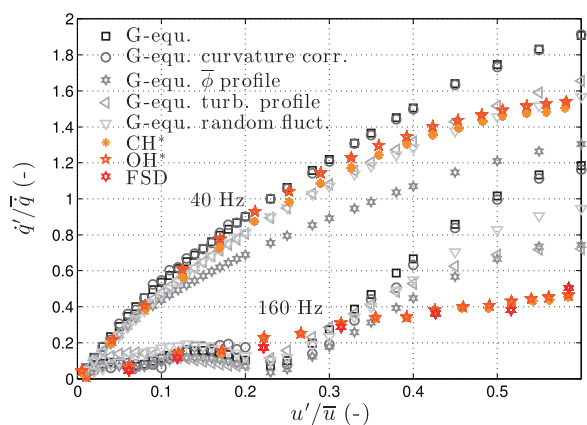


Figure 5. The numerically predicted saturation behaviour of the heat release as a function of forcing amplitude is compared with experiments.

General trends of the instantaneous measured heat release rates (see Balachandran,¹⁴ pp.176) are captured with the numerical approach and analytical flow model, as shown in Figure 6 for different forcing amplitudes at a frequency of 40 Hz. The simulations predict, in contrast to the experiments, higher maxima and less heat release in between peaks. This discrepancy can be related to the neglected flow recirculation and the temperature distribution used in the computations. The experimental measurements exhibit, in contrast to the simulations, significant cycle-to-cycle variations, which might be induced due to unsteady flow features. Further, dispersive effects translating the locations of the peaks can be observed in the experimentally measured heat release, which may be caused by large-scale turbulence.

3. Flame describing functions

First, we clarify the individual impact of the simplistic flow and perturbation models on the estimated FDF, which is illustrated in Figure 7. Considering only velocity perturbations (i.e. no equivalence ratio perturbations), Figure 7(a), the highest gain occurs at zero frequency and decays rapidly with small regular oscillations at approximately every 80 Hz. The velocity perturbation amplitudes depend linearly on the forcing amplitude (see equation (10)) so the gain is constant with amplitude.

Considering only equivalence ratio perturbations (i.e. no velocity perturbations in the combustion chamber^b), a more elaborate gain pattern can be observed, as shown in Figure 7(b). Dominant features are the high magnitude peaks at low forcing frequencies, a linear regime at low forcing amplitudes, and a regime exposing different heat release characteristics at high forcing amplitudes when the local equivalence ratio can become close to the stoichiometric ratio. At intermediate forcing amplitudes, an inclined gain interference pattern can be observed.

Combining the effects of velocity and equivalence ratio perturbations causes essentially the same gain pattern as that without velocity perturbations, but with an additional horizontal interference pattern (which is notable especially at high forcing amplitudes comparing the 0.25 and 0.4 gain iso-contours for the corresponding cases shown in Figure 7(b) and (c)). Thus, velocity perturbations affect the gain indirectly (with the potential flow model) by influencing equivalence ratio perturbations with respect to the flame front rather than generating heat release oscillations directly. The frequency of this interference effect is governed by the phase relation between velocity and equivalence ratio perturbations. Figure 7(d) shows that shifting the injection location closer to the burner orifice and altering

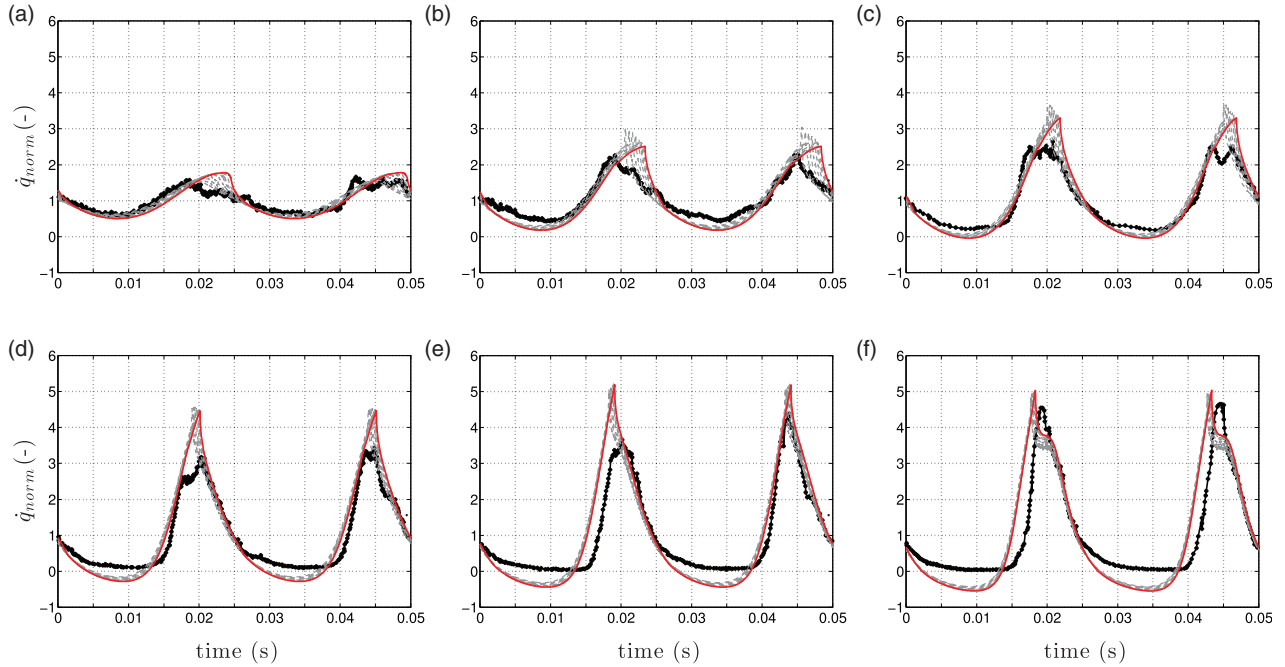


Figure 6. Comparison of the numerically estimated normalised heat release rate \dot{q}_{norm} (red) for different forcing amplitudes with experimentally measured data (black) (see Balachandran,¹⁴ pp.176) for a mean equivalence ratio $\bar{\phi}$ of 0.55 and a forcing frequency of 40 Hz. The grey dashed lines indicate the flame curvature effects. (Negative heat release rate values are possible due to the normalisation chosen by Balachandran¹⁴; $\dot{q}_{norm} = 2 \cdot \dot{q}(t)/\bar{q} - 1$.) (a) $F_A = 8\%$, (b) $F_A = 17\%$, (c) $F_A = 25\%$, (d) $F_A = 36\%$, (e) $F_A = 45\%$, and (f) $F_A = 54\%$.

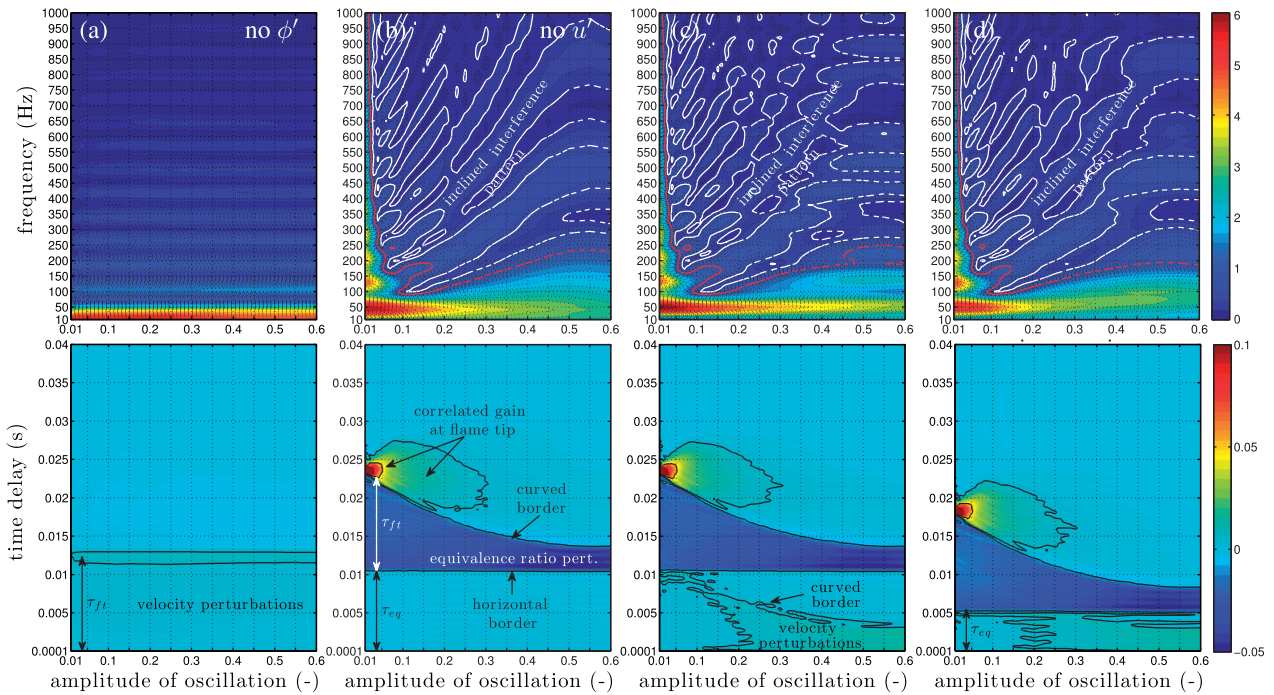


Figure 7. The flame describing function gain and the time delay coefficients for a mean equivalence ratio $\bar{\phi}$ of 0.55 are illustrated for different modelling procedures: (a) only the velocity perturbations (the gain is upscaled by a factor of four for this case), (b) only equivalence ratio perturbations, (c) velocity and equivalence ratio perturbations, and (d) velocity and equivalence ratio perturbations with fuel injection location at $z_{inj} = 27.5$ mm (closer to the burner) are considered. The number of time delay coefficients is 800, where $\Delta\tau$ is 0.05 ms. (Dashed 0.2, 0.45 (white), and 1.0 (red) iso-contours are added to indicate the inclined interference pattern and the linear regime.)

thereby the phase relation decreases proportionally the frequency of this horizontal interference pattern.

The time delay coefficients (as defined in equation (2)) enhance physical interpretation of the FDF. These show the amplitude of the heat release at a range of times after the reference velocity signal. From the convection time, the heat release location can be inferred, which can also be compared with images of the flame. In Figure 7(a), the higher values, which occur around $\tau_{fi} = 0.012$ s, correspond to the propagation time of the velocity disturbances to the flame tip. In this case, which has no equivalence ratio perturbations, the heat release modulation is generated mostly due to the flame tip motion caused by velocity perturbations. Due to the definition of the FDF in equation (1), a positive contribution due to velocity perturbations is expected.

For stiff fuel injection systems and quasi-steady forced oscillations, equivalence ratio perturbations and air stream fluctuations are proportional to each other, $\phi'/\bar{\phi} \sim -u'_{inj}/\bar{u}_{inj}$, where the index *inj* references the velocity *u* to the injection location. Because the velocity perturbations in the supply duct are caused by acoustic waves, the velocity fluctuations propagate instantly to the burner orifice, i.e. $u'_{inj}/\bar{u}_{inj} \approx u'_B/\bar{u}_B$. Thus, the heat release rate response provoked by velocity and equivalence perturbations are out of phase, which manifests itself as sign change in the time delay coefficients. Therefore, a horizontal border separates positive and negative coefficients at a time delay of approximately 0.01 s in Figure 7(b), which represents the intrinsic time delay accounting for the equivalence ratio fluctuation convection from the fuel injection location to the flame base. This intrinsic time delay, τ_{eq} , is altered by a shift of the fuel injection location, as shown in Figure 7(d).

The curved border visible in the time delay frames (bottom frames) of Figure 7(b) to (d) indicates the propagation time τ_{fi} of the equivalence ratio oscillations from the injector to the first flame-pinching event, which can be seen in Figure 9. This flame pinching leads to the disappearance of the high equivalence ratio perturbations that cause this event. Therefore, only low equivalence ratio perturbations remain on the flame front beyond this propagation time. These are in phase with the velocity perturbations and contribute positively to the coefficients at later time delays.

For very low forcing amplitudes, the heat release rate modulation is concentrated at the flame tip independently of the forcing frequency, because relatively small equivalence ratio perturbations do not lead to flame pinching and are therefore not completely burned before reaching the flame tip. Another way to look at this is that the time delay coefficients of one forcing amplitude represent an integration over all forcing

frequencies, which results in a high time delay coefficient associated with the equivalence ratio perturbations modulating the heat release rate at the flame tip.

When equivalence ratio fluctuations are present, it is worth noting that the velocity perturbations also contribute to the time delay coefficients. Elevated positive values are notable in Figure 7(c) and (d) (as compared with Figure 7(b)) at time delays lower than $\tau_{eq} \approx 0.01$ s, which mimic the negative shape with the curved border caused by the equivalence ratio perturbations at later time delays. The curved borders are separated by the intrinsic time delay, τ_{eq} , which governs the frequency of the horizontal interference pattern in the gain as $1/\tau_{eq}$. This demonstrates that velocity perturbations affect indirectly the heat release rate when equivalence ratio perturbations are present.

3.1. Gain distribution

The mean velocity and equivalence ratio define the overall distribution of the heat release rate amplification as functions of forcing amplitude and frequency, which is discussed further in the following paragraphs. The evolution for different equivalence ratios is shown in Figure 8, where the fuel injection location is unchanged. The horizontal interference pattern caused by the velocity perturbations can be observed for all mean equivalence ratios appearing at the same forcing frequencies.

Dominant high-amplitude peaks appear at low forcing frequencies (50–150 Hz), at the half wavelength of the equivalence ratio oscillation corresponding to the flame length. Therefore, maximal oscillations in the unsteady heat release are induced by the alternating appearing equivalence ratio fluctuations. For higher mean equivalence ratios, the flame length becomes shortened and therefore the frequency at which this peak occurs is increased. Further, this dominant peak is widened over a larger forcing frequency range for higher mean equivalence ratios. The horizontal interference pattern caused by the velocity fluctuations splits this dominant gain elevation at low frequencies for higher mean equivalence ratios ($\bar{\phi} > 0.7$).

At low forcing amplitudes, the equivalence ratio perturbations are too small to cause flame pinching and the foremost modulation of heat release is generated by equivalence ratio perturbations at the flame tip. When the wavelength of the equivalence ratio perturbations on the flame front is a multiple of the flame length, a maximum (crest) of the equivalence ratio perturbation disappears at the flame tip and a maximum equivalence ratio perturbation arises at the flame base (see also Shreekrishna et al.²⁵). These effects balance in terms of heat release rate generation, which evolves therefore relatively constant over a forcing cycle. In contrast, when the high equivalence ratio perturbations on the flame front

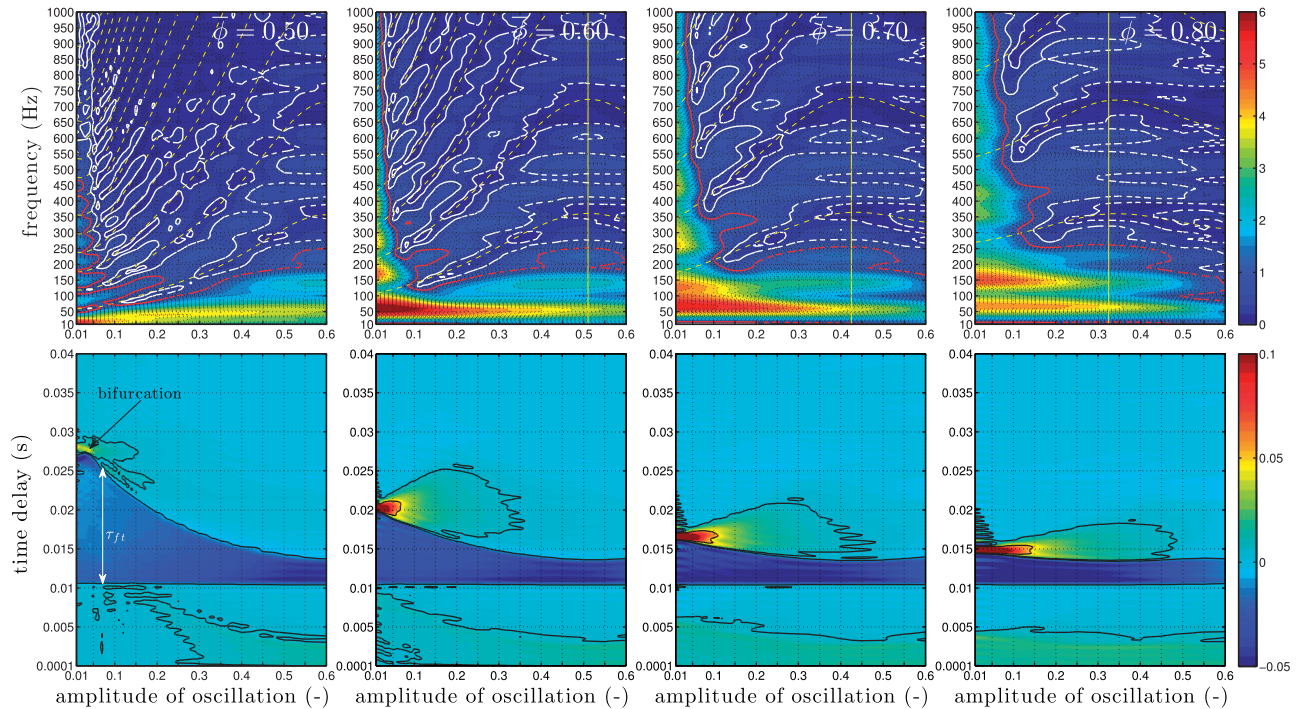


Figure 8. Flame describing function gains and time delay constants for different mean equivalence ratios. The vertical yellow lines indicate forcing amplitudes for which the flame speed of the perturbations reaches a maximum. The dashed yellow lines show the relation n/τ_f , where n is number of equivalence ratio maxima propagating on the flame.

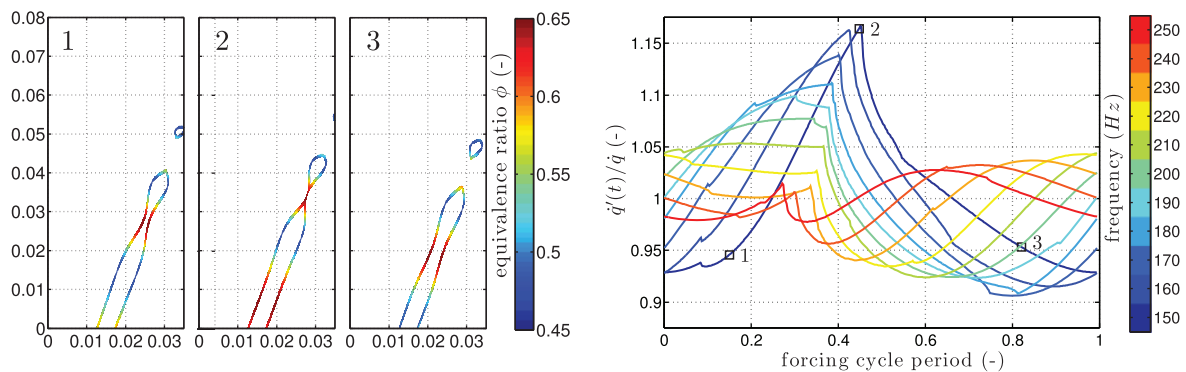


Figure 9. The flame front coloured by the equivalence ratio for a forcing amplitude of $F_A = 15$ is illustrated to the left for a mean equivalence ratio $\bar{\phi}$ of 0.55 and a forcing frequency of 150 Hz. To the right, the evolution of the heat release rate over one forcing cycle is shown for a frequency range. (The squares with numbers indicate the instants (left) to the overall heat release rate (right)).

form odd multiples of one half, a maximal modulation of the unsteady heat release is induced. This leads to high gain responses and a regular spaced pattern can be observed in this linear regime at low forcing amplitudes. The importance of individual equivalence ratio maxima is reduced with the number of extrema existing on the flame front and this regime becomes narrower with increasing forcing frequency.

The flame speed is low for mean equivalence ratios below 0.50. Therefore, the flame is impractically

elongated and penetrates the combustor walls. Hence, the importance of the heat release modulation at the flame tip diminishes. Equivalence ratio fluctuations generate a higher heat release rate response, when the wavelength matches the geometrical constrains of the burner. At higher forcing amplitudes, the flame speed increases and the flame becomes short enough that the fronts interact before penetration.

Interesting to note is the manifestation of the wall interaction in terms of time delay coefficients, where the

high peak value due to flame tip modulation is replaced by a bifurcated value distribution.

An inclined interference pattern generated by equivalence ratio fluctuations and flame pinching can be observed in Figure 8, which is illustrated quantitatively in Figure 9 by showing the heat release rate over one forcing cycle at constant forcing amplitude. Abrupt alterations of the unsteady heat release can only be provoked by events in which the flame front disappears suddenly, e.g. flame/wall interactions or pinching effects. Thus, flame pinching is the mechanism generating the cusps visible in Figure 9. On the other hand, the appearance of equivalence ratio patterns at the flame base and their propagation on the flame front change the heat release rate continuously.

The inclined interference pattern continues beyond the linear regime, since these patterns are generated by principally the same mechanism. However, flame pinching occurs within the inclined interference pattern region but not in the linear regime. Figure 9(2) shows that a maximal instantaneous heat release is generated when a maximal number of high equivalence ratio perturbations are burning on the flame front. The flame is pinching and a high equivalence ratio perturbation is convecting on the flame base. By the instant shown in Figure 9(3), the high equivalence ratio perturbation causing the pinch-off is burned and a low equivalence ratio perturbation is propagating at the flame base. This situation causes a very low heat release rate. Therefore, a maximal heat release modulation is reached. The inverse effect takes place (see the heat release rate at 240 Hz) when a flame pinching occurs while a low equivalence ratio perturbation is propagating at the flame base.

The inclined interference pattern is caused by the interaction of at least two equivalence ratio perturbation maxima. The number of multiple equivalence ratio perturbation maxima that can propagate on the flame surface is smaller for higher forcing amplitudes and mean equivalence ratios because flame pinching and therefore the disappearance of peak equivalence ratio perturbations occur after shorter convection times. Hence, the forcing frequency needs to be higher for such events to occur as compared with lower forcing amplitudes or mean equivalence ratios, which cause the inclination of this interference pattern.

Another way of understanding the formation of the inclined interference pattern can be attained by analysing the time delay distributions. The earliest flame-pinching event for a forcing amplitude is characterised by the time delay τ_{fi} and all the maximum crests of equivalence ratio perturbations on the flame are burned by this time. When the forcing frequency is a multiple of the inverse time delay, i.e. $f = n/\tau_{fi}$ (where n is the number of equivalence ratio maxima propagating on the flame), the wavelength of the equivalence ratio

perturbations is a multiple of the distance from the burner orifice to the earliest flame-pinching event. Therefore, the relation $f = n/\tau_{fi}$ characterises the minima of the inclined gain interference pattern, which is shown by dashed yellow lines in Figure 8(b).

Local equivalence ratios can become close to and even larger than unity for high forcing amplitudes. The sensitivity of the local enthalpy release and flame speed on the equivalence ratio differ on the lean and rich combustion side (see also Shreekrishna et al.²⁵). The flame speed reaches a maximum at approximately stoichiometric combustion and decays for lower or higher equivalence ratios, while the heat of reaction exhibits only minor dependence beyond stoichiometric combustion. Since these two mechanisms govern the gain amplification caused by equivalence ratio perturbations, the gain pattern reduces beyond this point (indicated by vertical yellow lines in Figure 8) where the equivalence ratio impact saturates and the gain decays rapidly thereafter. This is even more visible in the time delay coefficient distribution. As can be seen in Figure 8, the minimal time span until flame pinching occurs is independent of the mean equivalence ratio. However, the forcing amplitude at which it takes place changes with the mean equivalence ratio. At higher forcing amplitudes than this point, the time delay coefficient amplitudes decay rapidly.

The impact of mean velocity alterations is similar but opposite to the impact of mean equivalence ratio modifications. The mean velocity affects the flame length and thereby the propagation distance of an equivalence ratio perturbation until the flame pinches.

3.2. Further modelling

The high amplification of the heat release rate oscillation at low forcing amplitudes, generated due to correlated motion of the flame tip, is unrealistic for a turbulent flame. Several additional modelling strategies can be employed to overcome this problem, but remain with the computational efficiency of the analytical velocity model. The impact of perturbation convection in the supply duct, stochastic fluctuations at the flame, and flame curvature effects are addressed here.

Applying a radially non-uniform equivalence ratio perturbation can be caused by non-equally distributed fuel injection, which reduces symmetry of the flame set-up. Thereby, the coherence of the flame response at the flame tip and flame-pinching events is reduced. This causes a significant reduction of the gain, as shown in Figure 10(a), where a cosine distribution^c has been employed. Figure 5 illustrates that the impact on the gain is seen especially at large forcing amplitudes.

The convection in the duct distorts the equivalence ratio perturbation profile discharging at the burner

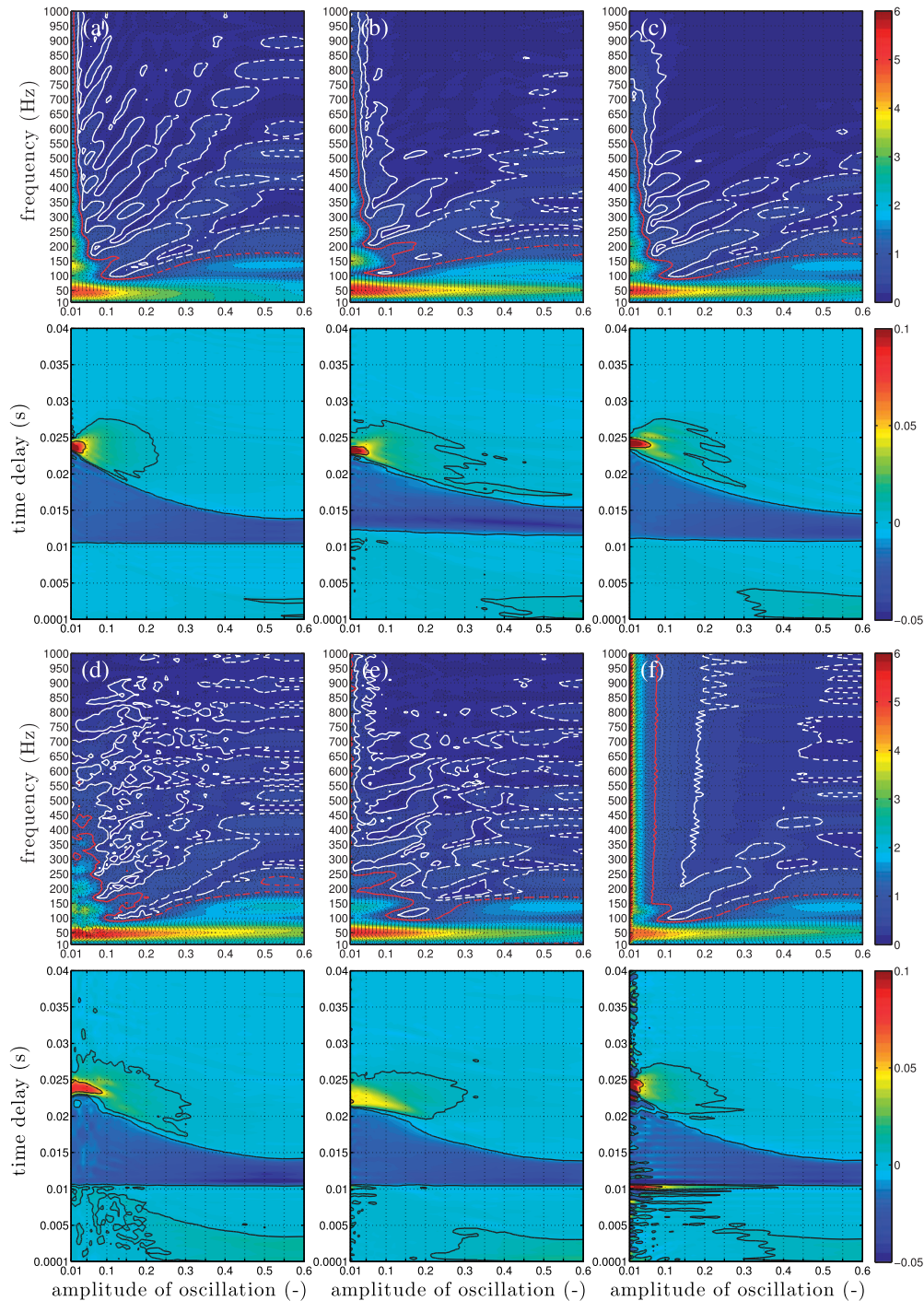


Figure 10. The effect of an asymmetric equivalence perturbation profile (a), a turbulent flow profile in the duct (b), stochastic perturbations in the supply duct (c), flame curvature effects (d), high (e) and low (f) frequent stochastic perturbations in the combustion chamber on the flame describing functions are illustrated for a mean equivalence ratio $\bar{\phi}$ of 0.55.

orifice. Incorporating the convection with a turbulent flow profile²⁶ into the modelling approach,^d the boundary layers delay the arrival of the equivalence ratio perturbations at the flame front. Therefore, the intrinsic time delay, τ_{eq} , is increased, as can be seen in Figure

10(b). Further, the distribution of equivalence ratio perturbations leads to a flame elongation, which causes a shift of the inclined interference gain pattern towards higher forcing frequencies. The coherence of the heat release response and oscillations due to the

inclined gain interference pattern are reduced, which is more evidently visible in Figure 5. It was observed that the impact on the gain is highly dependent on the particular turbulent flow profile imposed. A laminar flow profile can even increase the gain.

Stochastic fluctuations (of 10% of the mean velocity) imposed on the top-hat flow in the supply duct each time step disperse the equivalence ratio perturbations. Therefore, the gain is reduced as shown in Figure 10(c), which can be especially noted at high forcing frequencies.

Locally high curvature of the flame front causes the flame speed to increase, which occurs especially at the flame tip and with flame-pinching events. Flame wrinkling is damped when the curvature effects are taken into account, which occurs foremost at high forcing frequencies. At very low forcing amplitudes, the heat release rate modulation is primarily generated at the flame tip (with the present, analytical velocity model). Hence, it is expected that the heat release gain is dispersed in these regions when curvature corrections are considered, which can be observed in Figure 10(d).

Stochastic fluctuations can be imposed frequently (altered each time step) or infrequently (imposed over several time steps) in the combustion chamber, where the fluctuation amplitude has been assumed to increase with the radial distance from the burner orifice and reach 10% of the mean velocity at the flame tip. Frequent stochastic fluctuations disperse the gain and cause a similar gain pattern as obtained considering flame curvature effects. It is worth noting that the linear regime is extended to higher forcing amplitudes.

Infrequent stochastic fluctuations imposed in the combustion chamber additionally amplify the gain, since the velocity fluctuations are not contained in the reference velocity u'_B . As shown in Figure 10(f), these infrequent stochastic fluctuations overlay the gain generation at frequencies beyond the first gain minima. This manifests as a high and low peak at the intrinsic time delay indicating that the addition acts as hydrodynamic source.

4. Limit cycle prediction

Information-rich FDFs have been obtained with the aim of predicting thermoacoustic limit cycles more accurately. An acoustic network approach is used for limit cycle prediction, which has been described in detail by Stow and Dowling.⁵ Essentially, the thermoacoustic problem is separated into propagation-like sections, which are linked by jump conditions. The heat release response of the flame represents one of these jump conditions and is modelled by the sum of time delays approach described in equation (2). The governing equations are decomposed into mean and

perturbation contributions, while the latter are reformulated in terms of characteristic waves. These perturbations are propagated through the network, starting from known inlet conditions towards the outlet conditions. The state of the wave perturbations will not always satisfy the outlet boundary condition and therefore this perturbation exhibits a positive or negative growth rate. When the outlet boundary condition error vanishes for a wave perturbation with a non-zero amplitude and zero growth rate, a limit cycle is found. The limit cycle is stable when the growth rate decays with increased forcing amplitude and is unstable otherwise.

Many unstable thermoacoustic modes with positive growth rates can be observed in Figure 11(a) at low forcing amplitudes when flame curvature effects are neglected. These arise due to the high gain estimated in the linear regime and the steep phase decay. The inclined interference pattern causes the growth rate of the thermoacoustic modes to oscillate. Nonetheless, a limit cycle at a frequency of approximately 350 Hz is predicted, which is in agreement with the findings by Balachandran,¹⁴ who quotes a frequency of 348 Hz. However, the growth rate of this mode oscillates due to the inclined interference pattern. An unstable mode manifests at 60 Hz, which has a long wavelength. Accounting for the room as part of the piping network leads to a significant reduction of the growth rate for this mode.

When the equivalence ratio perturbation is non-uniform, Figure 11(b) shows that the estimated boundary condition error distribution is similar to that for a uniform equivalence ratio perturbation. However, the limit cycles establish at lower forcing amplitudes due to the reduced gain.

Modelling the supply duct convection with a turbulent flow profile leads to a slight frequency shift of the limit cycle to 345 Hz and increases its amplitude (see Figure 11(c)). The reduced gain oscillations observed in Figure 5 let the unstable mode appear nearly continuously over the forcing amplitudes.

Considering flame curvature effects does not change the estimated limit cycle frequency (as shown in Figure 11(d)) but does change its amplitude. Further, fewer unstable modes are seen with low oscillation amplitudes, although they remain unstable until higher amplitudes. These differences can be explained by comparing Figure 7(c) and Figure 10(d) more thoroughly. It can be noted that the gain decays rapidly to low values at low oscillation amplitudes when flame curvature effects are not considered. In contrast, the gain is initially lower for low oscillation amplitudes but remains higher until higher amplitudes, due to flame curvature effects. Further, the inclined interference pattern (indicated by the overlapped gain iso-contours) shifts towards higher

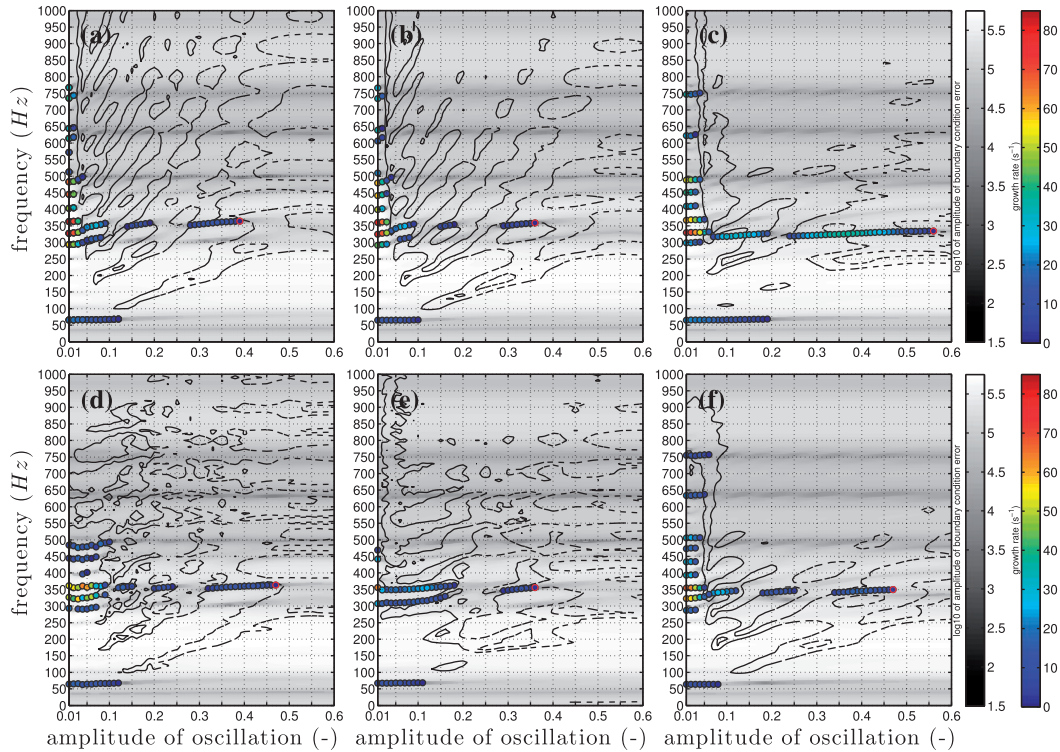


Figure 11. The 0.2 and 0.45 gain contours are overlapped on the logarithmic boundary condition error at the outlet as a function of frequency and non-linear oscillation amplitude at the flame, where the equivalence ratio $\bar{\phi}$ is 0.55 and the combustor length is 350 mm. Modes with positive growth rate are indicated as circles and the limit cycle is marked red. The reference case with time delay modelling is shown in (a). The impact of a radially non-uniform equivalence ratio perturbation and turbulent flow profile in the supply duct is shown in (b) and (c), respectively. Flame curvature effects are considered in (d). The effect of stochastic flow fluctuations in the combustion chamber and in the supply duct is plotted in (e) and (f), respectively.

oscillation amplitudes accounting for flame curvature effect, which leads to the increase of the predicted limit cycle amplitude.

Frequent stochastic fluctuations, which are imposed each time step, generally reduce the gain. Figure 11(e) shows that this reduction leads to fewer unstable modes when the stochastic fluctuations are imposed in the combustion chamber. When fluctuations are imposed in the supply duct (see Figure 11(f)), the distribution of modes with positive growth rates remains similar to the distribution without curvature corrections. Also, the inclined interference pattern is shifted to higher forcing amplitudes with this approach, which translates limit cycles to higher amplitudes.

Unsteady heat release oscillations can only add energy to the acoustic field when they are sufficiently in phase with the pressure oscillations. With a steep phase decay of the FDF, this condition is easily met over a range of frequencies. Figure 12 shows the predicted phase behaviour of the FDFs considering flame curvature effects, an equivalence ratio profile, a turbulent flow profile in the supply duct, and stochastic fluctuations in the combustion chamber. It can be noted that the phase decay is less

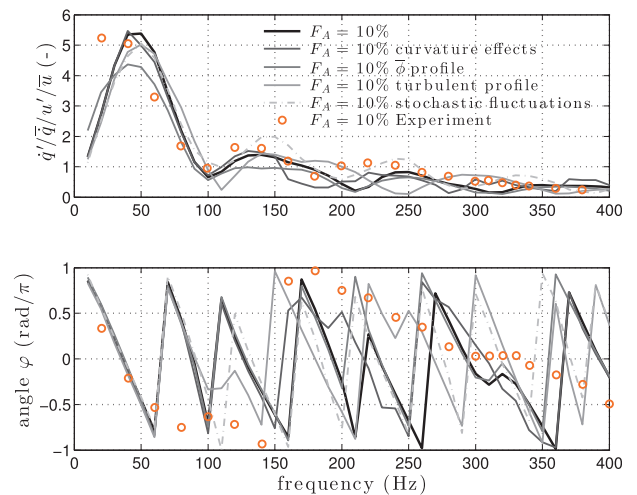


Figure 12. Quantitative comparison of the flame describing functions at a constant forcing amplitude F_A of 10%.

step when a turbulent flow profile is employed to connect the equivalence ratio perturbations in the supply duct. At approximately 350 Hz, the differences in the phase lag are small between the modelling approaches

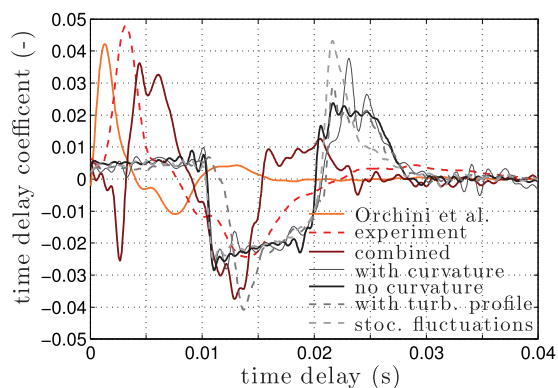


Figure 13. Comparison of time delay coefficients obtained from simulation data, experimental data by Balachandran,¹⁴ and data by Orchini and Juniper.¹⁵ Additionally, the results of a *combined* approach are illustrated, which connects the handling of equivalence ratio perturbations presented in this work and the flow model suggested by Orchini and Juniper.¹⁵ The mean equivalence ratio $\bar{\phi}$ is 0.55 and the forcing amplitude F_A is 10%.

and the dominant limit cycle is predicted at this frequency with all FDFs. However, the predicted limit cycle amplitudes vary significantly depending on the modelling approaches used.

5. Discussion

Figure 13 summarises the challenges of modelling imperfectly premixed flames with complex shapes by comparing the time delay coefficients of experimental data and G -equation models. The time delay coefficients of the experimentally obtained data by Balachandran¹⁴ exhibit a narrow high-amplitude peak at small time delays. Orchini and Juniper¹⁵ performed G -equation simulations of the same burner geometry, where only the large-scale flow structures were modelled and the influence of equivalence ratio perturbations neglected. Figure 13 reveals that the initial high peak is similarly represented as within the experimental data, while the large negative time delay coefficients are absent. This indicates that this first peak corresponds to heat release modulation caused by large-scale flow structures, which is not present in the estimation with the present model.

Equivalence ratio perturbations, which are the focus of this study, manifest themselves as negative coefficient distribution retarded by convection in the supply duct to higher time delays. The estimated amplitudes of the negative time delay coefficients are similar to those contained in the experimental data. Nevertheless, sharp transitions from positive to negative and negative to positive time delay coefficients are predicted with the present approach, which correspond to the convection time of equivalence ratio perturbations travelling in the supply duct and the duration of equivalence ratio

perturbations propagating on the flame front until the first pinching occurs, respectively. In contrast, the experimental data set exhibits a smooth transition.

Sharp time delay coefficient alterations lead to a steep phase decay, whereas smooth distributions result in a flat phase decay.¹² All modelling approaches estimate the phase response to be too steep. It seems therefore that this remains a significant challenge for low-order flame models.

Figure 3 shows that even the unforced flame shape is distorted by unsteady flow structures. Further, Figure 6 reveals that the instantaneous heat release of the experimental flame exhibits cycle-to-cycle variations due to unsteady flow. Thus, the heat release does not take place at the same location every cycle. Instead there are small-scale stochastic fluctuations and the response is dispersed. Sattelmayer²⁷ stresses the importance of turbulent dispersion and the resultant impulse response distribution over time delays on limit cycle prediction. Shin and Lieuwen²⁸ argue similarly and describe how stochastic flow fluctuations, on average, smooth wiggles of a premixed flame by modifying the linearised G -equation formulation. Accounting for small-scale stochastic fluctuations or flame curvature effects smooths the heat release response at the flame tip, especially at low forcing amplitudes. However, this does not improve the comparison to experimental data at a forcing amplitude of 10%.

Another modelling challenge is to deal with the artificially abrupt coefficient transition at the intrinsic time delay, τ_{eq} , corresponding to the equivalence ratio perturbation propagation in the supply duct (see also Albayrak et al.¹³), which is between 0.01 and 0.015 s in Figure 13. With the present approach (neglecting large-scale flow structures), a smooth transition in the time delay coefficients can only be obtained by modelling the dispersion and convection of mixture fraction perturbations in the supply duct. Alternatively, the smooth transition may be caused by the large-scale flow structures and consequential flame restoration,¹² as suggested by the fact that the time delay coefficients found by Orchini and Juniper,¹⁵ which included large-scale flow structures, have negative values.

For medium/large forcing amplitudes, only low equivalence ratio perturbations, which are in phase with the velocity perturbations, propagate far enough into the combustion chamber to be affected by large-scale flow structures. In the present investigation, the velocity perturbations influence the gain by redistributing the equivalence ratio perturbations, rather than by wrinkling the flame and causing a heat release modulation directly. Analogously, the large-scale incompressible flow structures could shift this contribution of the low equivalence ratio perturbations between 0.02 and 0.03 s to earlier time delays, thereby spreading them out.

The combination of the handling of equivalence ratio fluctuations presented in this work and the flow field description utilised by Orchini and Juniper¹⁵ underlines the importance of a realistic flow end equivalence perturbation model. This flow model improves significantly the phase decay prediction of the heat release as demonstrated in Figure 4. The analysis of the heat release response via the time delay coefficients (see Figure 13) reveals similar value distributions as obtained for the experimental data, i.e. a smoother value distribution as well as both contributions of hydrodynamic and equivalence ratio perturbations.

6. Conclusions

FDFs have been calculated for an axisymmetric M-flame using a level-set approach. The FDFs characterise the unsteady heat release caused by imposed velocity fluctuations over a wide range of forcing frequencies and amplitudes. Velocity fluctuations of the air cause equivalence ratio perturbations because the mass flow rate of fuel is constant, while that of the air varies. Equivalence ratio perturbations form at the fuel injector, which lies upstream of the dump plane, are convected down a duct. These are then convected to the flame front by a simple analytical flow; a spherical source term with oscillating source strength and an advanced low-order velocity model; a uRANS obtained mean flow with superimposed vortical flow structures. On the one hand, the FDFs are used to predict limit cycle amplitudes of thermoacoustic oscillations. On the other hand, they are also analysed by decomposing them into a sum of time delay coefficients, which reveals the physics behind the heat release characteristics of the flame.

The numerical results have been compared with experimental data. Reasonable comparison was achieved (even with a simplistic spherical velocity model) in terms of the heat release gain at constant forcing amplitudes and instantaneous heat release rates at constant forcing frequency. This indicated that the general distribution of the heat release gain can be estimated neglecting large-scale flow structures and turbulence, since these phenomena contributed little to the overall gain.

However, large-scale flow structures and turbulence influence significantly the phase decay and the gain oscillations due to the interference of equivalence ratio perturbations as they travel along the flame front. Broadband flow fluctuations smooth out these interference patterns and disperse the heat release response over wider ranges of time delays. These smoothly distributed time delay coefficients lead to a less steep phase decay of the heat release, which is more in line with experimental data. Therefore, the

flow field needs to be modelled realistically in order to obtain the correct heat release response.

In summary, the unphysically steep phase decay of the FDF in this model with analytic velocity representation leads to over-prediction of the number of unstable thermoacoustic modes, particularly at high frequencies. In addition, the inclined interference pattern (Figure 8), but which would be smoothed out in a turbulent flame, causes the growth rates around a given frequency to oscillate around zero as the amplitude varies (e.g. in Figure 11 around 350 Hz). Nevertheless, the predicted limit cycle frequency agrees well with experiments and the limit cycle amplitude, although quite strongly affected by the physical features of the model, is reasonably close to the experimentally observed amplitude of 0.6. A more physically velocity representation, mimicking the large-scale vortical flow structures, improves the phase decay prediction. This level-set approach, combining mixture fraction oscillations and appropriate velocity models therefore has proven to be a quick and reasonably accurate tool with which to calculate limit cycle amplitudes and frequencies of thermoacoustic oscillations for an axisymmetric burner.

Acknowledgements

This work was performed using the Darwin Supercomputer of the University of Cambridge High Performance Computing Service (<http://www.hpc.cam.ac.uk/>), provided by Dell Inc. using Strategic Research Infrastructure Funding from the Higher Education Funding Council for England and funding from the Science and Technology Facilities Council.

Declaration of Conflicting Interests

The author(s) declared no potential conflicts of interest with respect to the research, authorship, and/or publication of this article.

Funding

The author(s) disclosed receipt of the following financial support for the research, authorship, and/or publication of this article: This work was conducted within the EU 7th Framework Project Joint Technology Initiatives – Clean Sky (AMEL-Advanced Methods for the Prediction of Leanburn Combustor Unsteady Phenomena), project number: JTI-CS-2013-3-SAGE-06-009/641453.

Notes

- a. Enough information around the flame front needs to be considered to compute the spatial gradient of the G -field smoothly. The thickness of the flame tubes has been chosen with reference to the computational cell size, where $\beta = 3$ cells and $\gamma = \beta + 3$ cells.

- b. Only the equivalence ratio perturbation module is active, while the velocity perturbation module is switched off simulating this artificial case.
- c. A cosine distributed profile between 0 and $\pi/2$ with higher magnitudes at the inner radius is initially chosen such that the inner equivalence ratio value corresponds to the equivalence ratio perturbation amplitude calculated by equation (11) and the outer value is the mean equivalence ratio. Further, the profile is scaled in order to conserve the mean of the equivalence ratio perturbation amplitude.
- d. The numerical domain is extended to incorporate the entire supply duct, where the same discretisation scheme is employed as in the combustor domain to convect the equivalence ratio perturbations as passive scalar with the imposed profile.

References

1. Keller JJ. Thermoacoustic oscillations in combustion chambers of gas turbines. *AIAA J* 1995; 33: 2280–2287.
2. Tuttle SG, Chaudhuri S, Kopp-Vaughan KM, et al. Lean blowoff behavior of asymmetrically-fueled bluff body-stabilized flames. *Combust Flame* 2013; 160: 1677–1692.
3. Tuncer O, Acharya S and Uhm JH. Dynamics, NOx and flashback characteristics of confined pre-mixed hydrogen enriched methane flames. In: *ASME turbo expo 2007: power for land, sea, and air*, Montreal, Canada, 14–17 May 2007, pp.857–868. American Society of Mechanical Engineers.
4. Dowling AP. The challenges of lean premixed combustion. In: *Proc. international gas turbine Congress*. Citeseer, Tokyo, Japan, 2–7 November 2003, pp.1–7. Tokyo, Japan: Gas Turbine Society of Japan (GTSJ).
5. Stow SR and Dowling AP. Low-order modelling of thermoacoustic limit cycles. In: *ASME turbo expo 2004: power for land, sea, and air*. American Society of Mechanical Engineers, 2004, pp.775–786.
6. Macquisten M, Whiteman M, Stow S, et al. Exploitation of measured flame transfer functions for a two-phase lean fuel injector to predict thermoacoustic modes in full annular combustors. In: *ASME turbo expo 2014: turbine technical conference and exposition*. American Society of Mechanical Engineers, 2014, Vol. 4A: Combustion, Fuels and Emissions Düsseldorf, Germany, June 16–20 2014, pp.V04AT04A003–V04AT04A003. New York, USA: ASME.
7. Dowling AP. A kinematic model of a ducted flame. *J Fluid Mech* 1999; 394: 51–72.
8. Graham OS and Dowling AP. A low-order modelling of ducted flames with temporally varying equivalence ratio in realistic geometries. In: *ASME 2011 turbo expo: turbine technical conference and exposition*, Vancouver, British Columbia, Canada, 6–10 June 2011, pp.277–288. American Society of Mechanical Engineers.
9. Huber A and Polifke W. Dynamics of practical premixed flames, part i: model structure and identification. *Int J Spray Combust Dyn* 2009; 1: 199–228.
10. Huber A and Polifke W. Dynamics of practical premixed flames, part II: identification and interpretation of CFD data. *Int J Spray Combust Dyn* 2009; 1: 229–249.
11. Komarek T and Polifke W. Impact of swirl fluctuations on the flame response of a perfectly premixed swirl burner. *J Eng Gas Turbines Power* 2010; 132: 061503.
12. Blumenthal RS, Subramanian P, Sujith R, et al. Novel perspectives on the dynamics of premixed flames. *Combust Flame* 2013; 160: 1215–1224.
13. Albayrak A, Blumenthal R, Ulhaq A, et al. An analytical model for the impulse response of laminar premixed flames to equivalence ratio perturbations. *Proc Combust Inst* 2016; 36: 3725–3732.
14. Balachandran R. *Experimental investigation of the response of turbulent premixed flames to acoustic oscillations*. PhD Thesis, Cambridge, UK: University of Cambridge, 2005.
15. Orchini A and Juniper MP. Heat release response to forced flow oscillations of a low-order modelled laboratory scale dump combustor. In: *ASME turbo expo 2015: turbine technical conference and exposition*, Montreal, Quebec, Canada, 15–19 June 2015, pp.V04BT04A013–V04BT04A013. American Society of Mechanical Engineers.
16. Armitage C, Balachandran R, Mastorakos E, et al. Investigation of the nonlinear response of turbulent premixed flames to imposed inlet velocity oscillations. *Combust Flame* 2006; 146: 419–436.
17. Polifke W and Lawn C. On the low-frequency limit of flame transfer functions. *Combust Flame* 2007; 151: 437–451.
18. Hemchandra S. *Dynamics of turbulent premixed flames in acoustic fields*. PhD Thesis, Atlanta, Georgia, USA: Georgia Institute of Technology, 2009.
19. Kashinath K, Hemchandra S and Juniper MP. Nonlinear phenomena in thermoacoustic systems with premixed flames. *J Eng Gas Turbines Power* 2013; 135: 061502.
20. Orchini A and Juniper MP. Linear stability and adjoint sensitivity analysis of thermoacoustic networks with premixed flames. *Combust Flame* 2016; 165: 97–108.
21. Peng D, Merriman B, Osher S, et al. A PDE-based fast local level set method. *J Comput Phys* 1999; 155: 410–438.
22. Sethian JA. Evolution, implementation, and application of level set and fast marching methods for advancing fronts. *J Comput Phys* 2001; 169: 503–555.
23. Hartmann D, Meinke M and Schröder W. The constrained reinitialization equation for level set methods. *J Comput Phys* 2010; 229: 1514–1535.
24. Smereka P. The numerical approximation of a delta function with application to level set methods. *J Comput Phys* 2006; 211: 77–90.
25. Shreekrishna HS and Lieuwen T. Premixed flame response to equivalence ratio perturbations. *Combust Theory Model* 2010; 14: 681–714.
26. Okiishi TH. *Fluid velocity profile development for turbulent flow in smooth annuli*. PhD Thesis, Ames, Iowa, USA: Iowa State University, 1965.
27. Sattelmayer T. Influence of the combustor aerodynamics on combustion instabilities from equivalence ratio fluctuations. In: *ASME turbo expo 2000: power for land, sea, and air*, Munich, Germany, May 8–11 2000, pp.V002T02A003–V002T02A003. American Society of Mechanical Engineers.
28. Shin DH and Lieuwen T. Flame wrinkle destruction processes in harmonically forced, turbulent premixed flames. *J Fluid Mech* 2013; 721: 484–513.